Solid Earth Discuss., 3, 857–900, 2011
www.solid-earth-discuss.net/3/857/2011/
doi:10.5194/sed-3-857-2011

Solid Earth Discussions

Pore formation during dehydration of polycrystalline gypsum observed and quantified in a time-series synchrotron radiation based X-ray micro-tomography experiment

F. Fusseis[1,2,3,*], **C. Schrank**[1,2,3], **J. Liu**[1,2], **A. Karrech**[1,4], **S. Llana-Fúnez**[5], **X. Xiao**[6], **and K. Regenauer-Lieb**[1,2,3,4]

[1]Multi-scale Earth System Dynamics, Perth, Australia
[2]School of Earth and Environment, University of Western Australia, 35 Stirling Highway, Crawley WA 6008, Australia
[3]Western Australian Geothermal Centre of Excellence, Perth, Australia
[4]CSIRO Earth Science and Resource Engineering, Kensington, Australia
[5]Departamento de Geología, Universidad de Oviedo, Oviedo, Spain

[6]Advanced Photon Source, Argonne, USA
[*]now at Institut für Geologie, Mineralogie und Geophysik, Ruhr-Universität Bochum, Germany

Received: 20 September 2011 – Accepted: 26 September 2011 – Published: 21 October 2011

Correspondence to: F. Fusseis (florian@fusseis.at)

Published by Copernicus Publications on behalf of the European Geosciences Union.

Abstract

We conducted an in-situ X-ray micro-computed tomography heating experiment at the Advanced Photon Source (USA) to dehydrate an unconfined 2.3 mm diameter cylinder of Volterra Gypsum. We used a purpose-built X-ray transparent furnace to heat the sample to 388 K for a total of 310 min to acquire a three-dimensional time-series tomography dataset comprising nine time steps. The voxel size of 2.2 μm^3 proved sufficient to pinpoint reaction initiation and the organization of drainage architecture in space and time.

We observed that dehydration commences across a narrow front, which propagates from the margins to the centre of the sample in more than four hours. The advance of this front can be fitted with a square-root function, implying that the initiation of the reaction in the sample can be described as a diffusion process.

Novel parallelized computer codes allow quantifying the geometry of the porosity and the drainage architecture from the very large tomographic datasets (6.4×10^9 voxel each) in unprecedented detail. We determined position, volume, shape and orientation of each resolvable pore and tracked these properties over the duration of the experiment. We found that the pore-size distribution follows a power law. Pores tend to be anisotropic but rarely crack-shaped and have a preferred orientation, likely controlled by a pre-existing fabric in the sample. With on-going dehydration, pores coalesce into a single interconnected pore cluster that is connected to the surface of the sample cylinder and provides an effective drainage pathway.

Our observations can be summarized in a model in which gypsum is stabilized by thermal expansion stresses and locally increased pore fluid pressures until the dehydration front approaches to within about 100 µm. Then, the internal stresses are released and dehydration happens efficiently, resulting in new pore space. Pressure release, the production of pores and the advance of the front are coupled in a feedback loop. We discuss our findings in the context of previous studies.

SED

3, 857–900, 2011

1 Introduction

Since Heard and Rubey (1966) associated the dehydration of gypsum with a significant strength drop of the material, the reaction is often considered a model for the processes related to prograde devolatilization in tectonics and metamorphic geology. A wealth of studies was conducted to understand the mineralogy of the apparently simple reaction, but despite great efforts over the last hundred years or so, Charola et al. (2007), in their review of gypsum deterioration, had to point out that "a comprehensive approach to understand the true nature and behaviour of this ubiquitous compound [...] is still missing". There seems to be consensus that the dehydration of gypsum is a two-step process:

$$CaSO_4 \cdot 2H_2O \rightarrow (\alpha - /\beta -)CaSO_4 \cdot 1/2H_2O + 3/2H_2O \quad \text{(R1)}$$

$$CaSO_4 \cdot 1/2H_2O + 3/2H_2O \rightarrow (\gamma -)CaSO_4 + 2H_2O, \quad \text{(R2)}$$

in which gypsum, upon heating to temperatures larger than ~100° C first dehydrates into the metastable hemi-hydrate, which then dehydrates into γ-anhydrite (Bezou et al., 1995, Singh and Middendorf, 2007, Christensen et al., 2008, Jacques et al., 2009). The dehydration of gypsum is an anomalously slow process compared to the dehydration of other compounds containing crystal water (Charola et al., 2007).

This paper focuses on the first part of the reaction, the formation of hemi-hydrate from gypsum. Two hemi-hydrate varieties are distinguished on the basis of their specific surface area, crystal sizes, habit and surface topography of the crystals (Freyer and Voigt, 2003, 2009, Singh and Middendorf, 2007). Where the dehydration reaction occurs under a high partial water vapor pressure in acidic solutions, α-hemi-hydrate forms. β-hemi-hydrate results from dehydration under dry conditions or in vacuum. By comparison, Hildyard et al. (2011) identified euhedral hemi-hydrate crystals in polycrystalline gypsum samples that were dehydrated at low confining and effective pressures as α-hemi-hydrate (their experiments GYP37 and 38). The hemi-hydrate grains formed inequigranular, decussate aggregates.

SED
3, 857–900, 2011

Several models have been proposed as to how the reaction would progress in a polycrystalline sample (Olgaard et al., 1995; Ko et al., 1997; Miller et al., 2003; Wang and Wong, 2003). The model of Olgaard et al. (1995), refined in Ko et al. (1997), is probably based on the largest experimental dataset. Interpreting syn-experimental fluid expulsion measurements and micrographs made post-experimentally, they predicted dehydration to advance in three stages: a first stage, where the reaction commences throughout the sample but the released fluid is trapped in isolated pores, thus leading to high pore fluid pressures. In a second stage these pores are thought to interconnect and form a permeable network while fluid expulsion increases strongly. In a third stage, fluid expulsion decreases and the reaction comes to completion. Wang and Wong (2003) investigate this model numerically. They predict that dehydration occurs across a reaction front that propagates across a 25 mm long sample in less than 200 min. Porosity increases smoothly across the entire length of the sample. Even though Wang and Wong duplicate the fluid-expulsion curves of Ko et al. (1997) quite accurately, their results contrast with earlier descriptions of very sharp reaction fronts in dehydrating gypsum specimens by Stretton (1996). In her Plate 11.1, Stretton shows a partly reacted sample where the dehydration initiates across a narrow zone less than 50 micron wide.

Because the fluid volume (V_{fluid}) increases slightly more than the solid volume (V_{solid}) decreases during the reaction ($|\Delta V_{fluid}/\Delta V_{solid}|=1.3$), pore fluid pressure is considered critical for the reaction progress, the formation of drainage pathways and fluid escape (e.g., Heard and Rubey, 1966; Murrel and Ismail, 1976; Ko et al., 1997; Llana-Fúnez et al., 2011). Miller et al. (2003) propose a model where hydraulic fracturing resulting from fluid overpressure exclusively controls drainage. Applying Hacker's (1997) classification, the dehydration reaction is fluid-dominated and driven by a decreasing pore fluid pressure. Llana-Fúnez et al. (2011) associate fluid expulsion with reaction progress and show that a decreasing pore fluid pressure accelerates the reaction. It is known that the reaction is strongly pressure sensitive (McConnel et al., 1987; Karrech et al., 2011) and only proceeds where pore fluid pressures are relieved by water draining

SED
3, 857–900, 2011

from the reaction site (Miller et al., 2003; Llana-Fúnez et al., 2011). This renders the formation of permeable porosity critical for the reaction progress (Olgaard et al., 1995) and a hinge for all models of dehydration of polycrystalline gypsum.

All current models for dehydration of polycrystalline gypsum under drained conditions are based on the indirect assessment of reaction progress and porosity formation through fluid expulsion and the post-experimental, two-dimensional analysis of reaction fabrics in samples reacted to different extents. These are obvious limitations that were acknowledged by previous authors (Ko et al., 1997; Wang and Wong, 2003).

Here we apply a novel workflow that allows documenting the reaction progress in situ in three dimensions with high temporal and spatial resolution. We conducted a drained heating experiment in an X-ray transparent furnace and monitored reaction progress with synchrotron radiation based X-ray micro-computed tomography to acquire a volumetric time-series data set of the porosity evolution during dehydration. By documenting all pores larger than 2.2 μm^3 in volume, the tomographic time series data allow to precisely document the reaction. We quantify the progress of the dehydration front and analyse the organization of the drainage architecture in space and time.

Our data support a model where internally created pressures stabilize gypsum. The reaction only proceeds where these pressures can be relieved. This happens efficiently over a narrow dehydration front whose slow advancement can be described by a linear partial differential diffusion equation. A large interconnected pore cluster dominates the drainage architecture and links the exterior of our unconfined sample to the dehydration front at all times. Our observations suggest that under unconfined, drained conditions, hydraulic fracturing does not control the sample drainage. We conclude with an attempt to reconcile our observations with current models.

SED
3, 857–900, 2011

2 Materials and methods

2.1 Volterra gypsum

We cored a 2.3 by 8 mm cylinder from a block of Alabaster from Volterra, Italy. This polycrystalline material has become a standard for gypsum dehydration experiments (e.g., Ko et al., 1995; Oolgaard et al., 1995; Miller et al., 2003; Llana-Fúnez et al., 2011). Stretton (1996) determined a mean grain size of 120 micron, using a line intercept method on thin sections.

We used the intercept software of Launeau et al. (2010) to determine mean grain size and to analyse shape anisotropy in both secondary electron images taken from polished sections and photographs of thin sections acquired under polarized light and with crossed polarisers. The mean grain size of Volterra gypsum is between 45 and 123 µm (Table 1). Using this grain size interval, we estimate that the imaged part of our sample contains between 10 000 and 60 000 grains. Thin sections reveal that the material can be fairly heterogeneous locally (Supplement, Fig. 1). The aspect ratios of shape-fabric ellipsoids range from 1.09 to 1.52, indicating local shape-preferred orientations. Pockets of platy high-aspect ratio gypsum crystals were found to cover areas a few square millimetres in size (Supplement, Fig. 1). We have no indication that our tomographic sample is composed of grains of this size.

2.2 Synchrotron tomography

We used synchrotron radiation based X-ray micro-computed tomography (SRµCT) to document the progress of gypsum dehydration in 3 dimensions. SRµCT is based on two-dimensional digital radiographs that record the attenuation of coherent X-rays penetrating a sample. The attenuation of X-rays is a material property related to density; hence in compositionally heterogeneous samples the recorded X-ray absorption varies spatially. Radiographs shot from changing viewpoints are combined, using reconstruction algorithms, in a three-dimensional model of the distribution of different materials in

SED
3, 857–900, 2011

a specimen (e.g. Stock, 2009), in our case gypsum, hemi-hydrate and pores. During reconstruction, the spectrum of absorption values recorded in a sample is mapped into a 32-bit gray value space (2^{32} gray levels mapped into the numeric interval from –0.008 to 0.008). Several tomographic datasets acquired at different points in time from the same dehydrating polycrystalline gypsum sample can be merged in a four-dimensional (i.e. a time series) dataset.

Microtomographic data were collected at the bending magnet beam line 2-BM at the Advanced Photon Source, Argonne National Laboratory, USA. A double multilayer monochromator of 1.5 % bandwidth provided 27 KeV X-rays; images were collected in transmission mode by a CCD camera behind the sample in the hutch configuration. Data were collected through rotating the samples in steps of 0.125° over 180°. The acquisition time for each data set was about 25 min, which allowed for nine scans during the experimental run.

2.3 In-situ heating experiment

For the experiment, we used an X-ray transparent furnace that was installed within the tomographic setup (Fig. 1). The furnace consists of a hollow cylinder, made from Al_2O_3 ceramic, 10 × 30 mm in dimension, with a lid to limit the heat loss. The wall thickness of the cylinder is 1.5 mm. X-rays are allowed to penetrate the sample through two uncovered rectangular windows (4 × 4 mm) 3 mm from the bottom edge of the furnace. Two heating wires, coiled around the cylinder above and below the windows, heat the furnace. The sample, which was glued to a 25 × 25 × 13 mm Al-Si ceramic block at its base, was inserted into the furnace from the bottom. The ceramic base block insulated the rotation stage from the heat above. We rotated the entire lower assembly, which included the stage, the base block and the sample, for data acquisition. A thermocouple was mounted to the base of the sample cylinder. For all glued connections (heating coil and sample mounting, thermocouple installation) we used high-temperature Sauereisen No. 7 cement.

SED
3, 857–900, 2011

We heated the sample to 388 K for a total of 310 min (Supplement, Fig. 2). The experiment began with short heating periods (1, 2, 3 and 4 min), followed by five heating periods of 60 min each. In between each heating period, the reaction had to be suspended for data acquisition, and the sample was passively cooled to 323 K in about 2–3 min (Supplement, Fig. 2). After each scan, the furnace was heated to reaction temperatures in 46 s (ramp rate 150° min^{-1}). Before and after data acquisition, the sample experiences temperature fluctuations of 65 degrees that propagate through the cylinder. The time it takes for the sample to equilibrate thermally after each scan can be calculated using the thermal diffusion length scale (Clauser and Huenges, 1995, Regenauer-Lieb and Yuen, 2004): $t = 4r^2/D_T$ where t is the time scale, r is the sample radius and D_T is the thermal diffusivity. For a thermal diffusivity of gypsum of 0.285×10^{-6} m^2 s^{-1} (Clauser and Huenges, 1995) and a sample radius of 1.15 mm this indicates thermal equilibration in less than 20 s. This allows us to conclude that diffusion of heat (i.e., a thermal gradient) does not influence the kinetics of the reaction in our sample. All times given in the further text are minutes at 388 K, the reaction temperature.

A dummy sample was employed to train a Eurotherm 2404 controller to heat the specimen with a precision of about 1 degree. Only one thermocouple was used in the experiment, and we have no information on the temperature distribution in the furnace. While air was certainly circulating through the openings in the furnace we believe that the very responsive heater and the small dimension of the sample prevented major temperature gradients across the sample. We did, however, observe that the reaction progressed asymmetrically in the sample (see below). This possibly reflects some heat loss through the thermocouple and the cement that was used to hold it in place (see discussion).

2.4 Data processing and analysis

Three-dimensional models were reconstructed from 1440 tomographic projections/time step for all nine time steps of this study using Advanced Photon Source in-house

SED
3, 857–900, 2011

algorithms and facilities. Each projection image comprises 2048 × 1536 pixels in raw format and each reconstructed three-dimensional dataset is discretized into a stack of 1536 horizontal image slices with a vertical spacing of 1.3 microns. During 3-D rendering, these image slices are combined in a volumetric dataset consisting of 2048 × 2048 × 1536 voxel. The minimum effective pixel size achieved was 1.3 µm, yielding a volume of 2.2 μm^3 per voxel. All of our datasets proved of excellent quality, with a minimum of noise and artefacts. The data document a 2 mm section out of the upper half of the specimen cylinder, just above the thermocouple; the top of the cylinder is not included in the dataset.

The X-ray absorption of gypsum and hemi-hydrate proved sufficiently different from water and air to clearly distinguish pores from minerals, and the achieved spatial resolution is sufficient to do so (Fig. 2). It is difficult to distinguish gypsum and hemi-hydrate in the reacted part of the sample.

We use the term pore for any void space irrespective of the shape and size (cf. Sprunt and Brace, 1974). Due to their low X-ray attenuation, pores occupy the low end of the grey value histogram derived from a tomographic dataset (Fig. 3). We segmented pores from solids by binary thresholding. The process, which requires the determination of a critical threshold, separates all voxels into those that belong to pores and those that do not.

For binary thresholding, determining the correct threshold value is critical (Kaestner et al., 2008 and references therein). In our case the reaction affects the grey value distribution and we found that we could use these changes to accurately determine the threshold value (Fig. 3). For all time steps, we calculated histograms of the grey value frequency distribution from 180 million voxels that constitute a parallelepiped just off the centre of the sample cylinder (400 × 600 × 750 $voxel^3$ or 520 × 780 × 975 μm^3). As the reaction proceeded through the parallelepiped, hemihydrate and pores formed, and consequently voxels were reassigned amongst the 1024 bins constituting the histogram. Hemihydrate is slightly denser than gypsum; therefore voxels that were gypsum and become hemihydrate assume grey-values equal or greater than that of

SED
3, 857–900, 2011

gypsum. In the histogram, they will increase the "height" of the bright right shoulder (Fig. 3). On the other hand, pores, water- or gas-filled, have a much lower density than gypsum and hemihydrate. Therefore, voxels that were gypsum and turned into pores will attain grey values smaller/darker than that of gypsum and hemihydrate. They will increase the frequency of dark voxels and hence contribute to the dark left shoulder of the histogram (Fig. 3). This low-absorption shoulder is delimited by an intersection point of all histograms at a grey value of 0.00018 (inset in Fig. 3), which separates the brighter bins occupied by gypsum voxels from darker bins of pore voxels. We used this value to segment pores from gypsum and hemihydrate in all datasets.

All pores in the above-mentioned parallelepiped were analysed. We use the method of Liu et al. (2009) to label face-connected clusters of "porous" voxels as individual pores. We calculate the position, volume, surface, shape and orientation of each individual pore. In the datasets obtained prior to heating and after 10, 70, 130, 190, 250 and 310 min at reaction temperature, we determined frequency distributions for pore size, pore shapes, pore orientation and performed a percolation analysis.

We furthermore used a moving window method to analyse the porosity increase along a radius of the sample in the dataset obtained after 10, 70 and 130 minutes. We migrated a 20 × 400 × 750 voxel large box along the x-axis across the dehydration front described below. The radius was chosen so that the front was crossed in sections with low curvature. We used a step size of 1 voxel, and quantified the porosity in each box. We ascribe the fact that, in this analysis, we recorded porosity values that exceed the theoretically expected 29 % to result from the narrow sampling box combined with a locally heterogeneous distribution of porosity.

Two error sources affect SRμCT data: errors introduced during data acquisition and reconstruction (Banhart, 2008) and the common discretization error of raster data (e.g. Arns et al., 2002). We estimated the combined error conservatively by assuming that the surface of each pore is subject to an uncertainty of ± one voxel with respect to the surface normal vector. Since the topology of pore space is very complex, we quantified this error empirically by a numerical dilation/erosion experiment: we expanded

SED
3, 857–900, 2011

and shrank each pore in the parallelepiped by one voxel on their outer faces (Liu and Regenauer-Lieb, 2011) and then quantified the respective changes in the data. Apart from returning error margins for our quantification, this test provides insight into the pore structure and we discuss the results below. We stress that these error margins significantly overestimate the true error.

The data were visualized using the imaging software Avizo Fire.

3 Results

The following chapter is subdivided into two parts: A first part (Subsect. 3.1) describes the two textural domains we identified in the data and the dehydration front that separates them. We quantified the advance of this front in the sample over time to assess the reaction progress through dehydration initiation. In a second part (Subsect. 3.2) we analyse the porosity evolution behind the dehydration front to characterize the drainage architecture in the sample and its evolution during the experiment.

3.1 Dehydration initiation

The tomographic data acquired of the partly dehydrated samples reveal two textural domains, separated by a narrow boundary (Fig. 2). The inner textural domain shows a relatively homogeneous X-ray absorption. Based on the histogram obtained from the unreacted sample (Fig. 3) the attenuation pattern in the inner domain is attributable to gypsum. The outer textural domain shows a more heterogeneous and wider absorption distribution resulting from abundant porosity in between the (denser) solid phases, gypsum and hemi-hydrate (Fig. 2). Over the course of our experiment the relative widths of these domains change and the narrow boundary separating them migrates steadily inwards from the periphery of the sample cylinder (Fig. 2).

We use the porosity, which is indisputably a result of the reaction, as a proxy for the onset of dehydration. As only very few pores were documented in the inner domain

SED
3, 857–900, 2011

(Fig. 2), we infer that, on the scale that we could resolve in the tomographic datasets, gypsum is stable there. Consequently we interpret the advancing boundary between the inner and the outer textural domain as a dehydration front that delimits the gypsum stability field spatially. The front marks the point where, on the scale of observation, gypsum becomes unstable and dehydration advances rapidly. The dehydration front itself exhibits a steep porosity gradient (Fig. 4). Porosity increases from between 2.7 and 6.8 % to about 30 % over a distance of 100–200 µm. The gradient remains similar over the duration of the experiment.

We tracked the progress of the dehydration front in two horizontal and two vertical tomography slices at times 3′, 6′, 10′, 70′, 130′ and 190′. We measured the cumulative radial propagation, $r_\alpha(t)$, of the dehydration front. $r_\alpha(t)$ denotes the distance that the dehydration front has travelled over the time t from the sample margin along a radial line of orientation α (Supplement, Fig. 3). The long axis of the cylindrical sample is defined as Z-axis. Radii are defined as lines in the plane normal to Z that connect the sample margin and the centroid of the unreacted domain. In horizontal slices, we determined $r_\alpha(t)$ in steps of 0.5° for the interval [0°; 360°] at a given height z_i. We chose horizontal slices located in the middle of the sample volume (at $\sim Z/2$) to avoid early interference with the dehydration front propagating inward from the top surface of the sample. The vertical slices represent the XZ- and the YZ-plane of the sample, respectively, and cover the entire height of the imaged sample volume. Hence, the orientations of the considered radii are 0° and 180° for the XZ-plane and 90° and 270° for the YZ-plane (Supplement, Fig. 3). In each vertical slice, radial progress was determined not only for two opposite orientations but also at different vertical positions. We used a vertical step size Δz of 13 micron for each pair of measurements (Supplement, Fig. 3). In addition, the temporal evolution of the proportion of dehydrating area with respect to total sample area was calculated for the horizontal slices (Supplement, Fig. 4).

The results show that the dehydration front propagates in a non-linear fashion (Fig. 5). It moves faster in the beginning of the experiment and slows down

SED
3, 857–900, 2011

subsequently. There is a marked asymmetry in dehydration front progress. The front moves faster on the right side of the sample in the XY-plane (i.e., the clockwise orientation interval [270°; 90°], Fig. 5a). In other words, the centroid of the unreacted domain does not coincide with the centroid of the sample cylinder.

We used a non-linear least squares method to fit the results with a linear diffusion function of the type

$$x(t) = D(t) \quad (1)$$

where $x(t)$ is distance of front to sample margin, D is a constant diffusivity, and t is time. We obtain a D of 8.29×10^{-11} m^2 s^{-1} with $r^2 = 0.71$ (Fig. 5c).

The initially smooth front exhibits a variable roughness with a trend to irregularities with higher amplitudes later during the experiment (Figs. 2 and 5a). The wavelength of these front indentations, 20 to 100 µm, is of the same order of magnitude as the mean grain size of the sample (cf. Table 1). None of the undulations persists beyond one hour. In cases, individual cusps become narrow plumes of micron-sized pores extending up to 200 µm into unreacted gypsum. In three dimensions, these "plumes" are irregular porous sheets that are usually directly connected to a large pore in the outer domain. In the very early stages of the experiment, we did observe an alignment of these plumes with some of the cracks described below. The plumes occasionally surround volumes that are left behind by the moving dehydration front. In these volumes, porosity increases with time.

Over the first three hours we found isolated crack-like features in the specimen. The width of these features is at the resolution limit, their longitudinal extent up to several hundred microns. They showed no preferred orientation. We did not see an increase in their number, or width, as the experiment progressed. Neither did we see any porosity associated with the features apart from a few very early pores following them at the periphery of the sample. Based on Stretton's (1996) observation that gypsum is very unlikely to crack but will rather deform crystal-plastically, even at moderate temperatures, we are uncertain whether these features are cracks. As they did not affect the reaction progress we do not consider them any further.

SED
3, 857–900, 2011

3.2 The outer domain: porosity and drainage architecture

3.2.1 Porosity

Visual inspection of the porosity in the outer domain indicates that the porosity consolidates rapidly once the front has passed (Supplement, Fig. 4). We quantified the temporal evolution of porosity in the parallelepiped to better understand this consolidation and the geometry of the dehydration architecture. The porosity evolution is summarized in Table 2 and Figs. 6 to 8.

The unreacted sample exhibits a porosity of 2.32 % (Fig. 6a), which is somewhat higher than the previously published figures for Volterra gypsum (0.5 %, Ko, 1993, 0.1 %, Stretton, 1996) and probably related to different measurement techniques. As the reaction front propagates through the parallelepiped, the total porosity increases. After 130 min, when the front has passed the parallelepiped, the porosity peaks at 25.67 %. The porosity then decreases slightly to 24.01 % over the next three hours. Both values are remarkably close to the theoretically predicted 29 % (e.g., Ko et al., 1997), which we consider an indication that the critical threshold used for segmentation of the data is appropriate.

The total number of pores is very high in the unreacted dataset (>2.1 million, Fig. 6b), increases at first as the dehydration front propagates into the sample (10 min) but then decreases to 0.53 million after 130 min. Over the next three hours it increases again to reach 0.63 million after 310 min, indicating that more pores accommodate slightly less porosity. The observed changes in total porosity and the number of pores once the front has passed (130 min) are subtle and within the discretization error. The datasets from the numerical expansion/shrinking experiment essentially mirror this evolution of the total porosity, despite the obviously quite different absolute values (Fig. 6a). Expansion reduces the total number of pores at all times, while shrinking increases them to a level above the original data after 130 min (Fig. 6b). This indicates that pores formed during the reaction are not isometric, so that shrinking leads to a break up into several smaller pores. Furthermore it shows that they are close enough to each other so that

SED
3, 857–900, 2011

expansion by just one voxel joins neighbouring pores.

The pores in the outer domain span a wide range of sizes, from one to a maximum of 43 million voxel. Porosity in the unreacted sample is comprised of a large number of very small pores (Fig. 7); pores smaller than 100 μm^3 make up more than 95 % of the total porosity (Fig. 8), with pores smaller than 5 μm^3 contributing more than 50 % of the porosity. During the experiment, the pore size frequency distribution evolves from the unreacted one until it assumes a characteristic shape and position after 130 min (Fig. 7). After that, the changes are subtle but marked by an increase of especially the smallest pores (inset in Fig. 8). While after 130 min the contribution of pores smaller 1000 μm^3 is only 6 % of the total porosity, the value increases to about 8 % after 310 min.

The dehydration-related porosity is characterized by the formation of one very large pore after 70 min (Fig. 9). This topologically very complex pore accounts for more than 90 % of the total porosity (Table 2, Fig. 8). It is four orders of magnitude larger than the second largest pore, intersects all faces of the parallelepiped and seems responsible for drainage of the volume. A visualization of this pore in a horizontal cross section shows that it connects the sample margin with the reaction front (Supplement, Fig. 4).

As indicated by the shrinking test, the pores formed during dehydration are not isometric and this does not change over the course of the experiment. We characterize the shape of a pore by its isotropy index (i_i), which is defined as $i_i = e_3/e_1$, with e_1 and e_3 being the largest and smallest eigenvalue, respectively, of the orientation matrix of a pore as defined in Liu et al. (2009). $i_i = 1$ denotes an isotropic shape, while "cracks" in the definition of Sprunt and Brace (1974) have ii equal to or smaller than 0.1.

For this analysis we only consider pores larger than 50 voxel to minimize shape artefacts due to the raster effect. We also excluded pores larger than 1200 voxel, as their shapes are too complex to be accurately described by the method (cf. Fig. 9). Our analysis shows that after 130 min 78 % of the pores have an isotropy index smaller than 0.5 but larger than 0.2 (Fig. 10). There is a tendency for larger pores to being more anisotropic. After 130 min only 0.6 % of all pores have isotropy indices equal to

SED
3, 857–900, 2011

or smaller 0.1. After 310 min, 0.4 % of pores have isotropy indices of 0.1 or smaller, whereas 80.1 % have isotropy indices between 0.2 and 0.5.

3.2.2 Drainage architecture

The grain shape analysis we conducted on Volterra alabaster indicated a slight shape-preferred orientation of grains (Table 1). To test the influence of such a pre-existing fabric on the evolving porosity, we determined the orientations of pores of three different size fractions (51–150 voxel, 151–300 and 301–450 voxel) at different times during the experiment. The orientation of a pore is represented by azimuth and dip angle of $e1$ with respect to the coordinate system (Fig. 2). Figure 11 illustrates the orientation of pores in the subsampled parallelepiped prior to heating, after 70 min and after 310 min. The orientations from the latter two datasets show the preferred alignment of pores along a great circle at an angle of about 30 degrees to the xz-plane, with a maximum close to the x-axis. Albeit weaker, due to the smaller of number of pores, this trend can already be seen in the sample prior to heating (Fig. 11a). In the datasets acquired during dehydration, pores of all three size-fractions follow this trend. The maximum density of e_1 orientations of the smallest size fraction (expressed through the contour lines in Fig. 11b and c) rotates, within the xy-plane, into the great circle between 70 and 310 min.

The cumulative pore size frequency distribution indicates that a single pore drains the volume soon after the dehydration front has migrated through a volume. We conducted a percolation analysis to investigate this observation further. Percolation here refers to the connectivity of pores (Stauffer and Aharony, 1994). A moving window method was used (Liu et al., 2009), where cubes of various side lengths (25, 50, 100 and 200 voxel) are moved through the segmented datasets with a step size of 5 voxel. For each cube position the porosity in the cube and pore connectivity in the principal directions of the coordinate system are determined. For a given cube size, the analysis yields the porosity frequency distribution for all cube positions (Fig. 12), as well as probability functions for percolation in the principal directions for all cube placements (Fig. 13).

SED
3, 857–900, 2011

The porosity frequency distribution illustrates how homogeneously porosity is distributed in the sampling volume (Fig. 12). The more heterogeneously porosity is distributed, the wider the porosity frequency distribution will be. Vertical lines mark the total porosities measured in the parallelepiped (Table 2) for reference. The distributions of porosities amongst the cube placements for the datasets from 130 to 310 min are narrow and have their maxima within 2.5 % of the measured total porosities. The frequency distributions derived from the 10′ and 70′ datasets reflect a comparatively large variability amongst the cubes, which is due to the circumstance that the dehydration front is still propagating through the parallelepiped at these times.

Probability functions for percolation in the three principal directions for each time step describe the time-dependent evolution of percolation in the parallelepiped. Each of the four diagrams in Fig. 13 compares the probabilities for percolation in a $50 \times 50 \times 50$ voxel cube with a given porosity for two successive time steps. It becomes evident that the differences between the probability functions for the three directions are subtle, particularly after 130 min, and cubes with a porosity of 20 % or more are percolating in all three directions with a probability of more than 90 %. However, cubes with porosities below ∼19 % are more likely to percolate in the x-direction.

4 Interpretation and discussion

In-situ SRμCT time-series experiments and their quantitative analysis provide a novel way of studying tectono-metamorphic processes, fluid-rock interaction and secondary porosity. Despite its comparatively simplistic setup, our experiment overcomes the "black box" limitations of previous experimental studies and maps a way towards the discrete characterization of metamorphic dehydration. Our results provide detailed insight into the advance of dehydration in polycrystalline gypsum, the porosity-forming mechanism and the influence of pre-existing fabric anisotropy on drainage.

SED
3, 857–900, 2011

4.1 Dehydration initiation

Confirming previous observations, our tomographic data show that the dehydration reaction propagates radially from the outer surface of the sample, where the water released during the reaction can escape, to the sample centre (Fig. 2, e.g. Ko et al., 1997; Miller et al., 2003; Llana-Fúnez et al., 2007). A dehydration front delimits the drained portion of the sample (Figs. 2, 4, 5) from an inner domain. In this inner domain no resolvable fluid drainage pathways are created and gypsum is essentially stable. The stability of gypsum ahead of the dehydration front can be explained with the well-known pressure-dependence of the reaction. Karrech et al. (2011) recently revised experimental data by McConnell et al. (1987) and showed that, at 388 K, gypsum is stable at pressures of >53 MPa. Karrech et al. (2011) demonstrate that the primary pressure source for reaction suppression in the sample interior derives from internal stresses due to the anisotropic thermal expansion of gypsum (cf. Ballirano and Melis, 2009).

Our analysis confirms that the reaction commences in the inner domain wherever water can drain into pre-existing pores or thermal cracks (Olgaard et al., 1995; Ko et al., 1997). We believe that the slightly increasing background porosity in the sample interior (Fig. 4) is the expression of such dehydration nuclei. As previously recognized, the resulting local increase in pore fluid pressure will help to suppress the reaction. However, our data also indicate that any pores that form remain largely below the resolution limit of about 1 micron, and run-away interconnection of such pore space does not occur. The reaction is suppressed until the dehydration front has approached.

We interpret that gypsum breakdown and pore formation are very efficient once the dehydration front has approached to within about 100 µm, or roughly one average grain diameter, which marks a critical length scale for the reaction. We postulate that the key processes during dehydration are intrinsically coupled in a feedback loop related to pressure changes across the dehydration front. At the dehydration front, the thermal-elastic internal and fluid-induced stresses are no longer in static equilibrium, and pore

SED
3, 857–900, 2011

fluid that was previously trapped in pores is released into the drainage system. The resulting pressure drop drives the reaction, i.e. the dehydration of gypsum, which produces new pore space and consequently advances the dehydration front.

As the reaction is controlled on the grain scale, this model does not explain the fluid expulsion behaviour observed by Ko et al. (1997). However, it seems also applicable to explain observations made during the dehydration of serpentinite (Llana-Fúnez et al., 2007). In our model, the feedback operates on a grain-by-grain basis and no run-away effects occur. The fluid expulsion rate is proportional to the rate at which the unreacted domain shrinks. Figure 4 shows that 50 % of the sample area in horizontal cross-section reacts within the first 17 min. Hence, the highest fluid expulsion rates are expected at the onset of the experiment. The lacking confinement of our sample, which leaves it free to drain through most of its surface, is the largest difference between our and previous studies. Other investigators generally applied at least some confining pressure and externally controlled pore fluid pressure (Olgaard et al., 1995; Ko et al., 1997; Miller et al., 2003; Llana-Fúnez et al., 2011). Both pressure sources control compaction in the outer domain and contribute to thermal-elastic internal stresses. This additional mechanical loading might explain the difference in fluid expulsion behaviour.

Our model is similar to the concept of Wang and Wong (2003), who proposed an empirical relationship between the dehydration rate and porosity generation. While their model captures many of the measurements of Ko et al. (1997), we do see discrepancies in the scales of the dehydration front and porosity evolution. Wang and Wong (2003) postulate a porosity increase of about 8 % over a sample length of 25 mm (cf. their figure 7b). However, similarly to Stretton (1996), our data clearly show a very narrow dehydration front with a steep porosity increase of up to 30 % over a distance of less than 150 µm (Figs. 2, 4). Whether this disparity is caused by our choice of a millimetre-sized sample or an oversimplification in the underlying empirical model of Wang and Wong (2003) remains to be clarified. In a companion paper (Karrech et al., 2011), we develop a theory that captures the advance of the dehydration front on the basis of the dissipative mechanisms underlying the above feedback, and successfully

SED
3, 857–900, 2011

reproduce both the sharp dehydration front and its progress over time.

In brief, this theory describes the advance of the reaction front as a pressure diffusion process, accounting for thermal-elastic internal and fluid-induced stresses in a coupled manner. The linear diffusion constant governing the advance of the dehydration front due to pressure diffusion can be derived from our experiment by fitting the front propagation data with Eq. (1) (Fig. 5b). We obtain a value of 8.29×10^{-11} m^2 s^{-1} ($r^2 = 0.71$). The spread of the data in Fig. 5b is due to the undulations of the dehydration front and its asymmetric progress (Figs. 2 and 5a). As discussed in the following section, both front undulations and asymmetric propagation are most likely a result of the lattice/fabric control of gypsum breakdown and porosity formation. The resulting data spread implies that our sample cannot be regarded as a homogeneous medium on the length scale of the sample radius. However, we calculated the percentage of reacted sample area in horizontal cross section over time assuming a perfectly concentric reaction progress and using the diffusion constant obtained here and compared it to the percentage of reacted sample area determined in the physical experiment. Theoretical prediction and measured data match very well (Supplement, Fig. 4). This might indicate that our small sample approaches statistical homogeneity with regards to microstructure at the scale of the entire sample cylinder. However, determining the representative elementary volume for Volterra alabaster is beyond the scope of this work. The diffusion constant determined here should therefore be understood as rough estimate with an uncertainty of plus/minus one order of magnitude (see also Fig. 5c). Nevertheless, it constitutes a material property than can be employed to predict the progress of the dehydration front in drained, unconfined gypsum.

4.2 Gypsum breakdown and porosity formation

We interpret the highly anisotropic gypsum lattice to control the actual breakdown process as well as the shapes of the pore nuclei in a similar way as it controls the formation of hemi-hydrate. Sipple et al. (2001) show that hemi-hydrate forms a pseudomorph after the parent gypsum crystal. Hildyard et al. (2011) observed the inheritance of a

SED
3, 857–900, 2011

crystal-preferred orientation in hemi-hydrate from parental gypsum and they employ Freyer and Voigt (2003), who predict a topotactic growth relationship between the two minerals. Finally, Finot et al. (1997) documented dehydration of gypsum in-situ and observed a remarkable mobility of water molecules along the (010) lattice planes, outlining preferred evacuation pathways that must have been provided by intracrystalline pores. Combining these observations, and considering the volume change that is involved in the formation of hemi-hydrate, it seems likely that pores that nucleate on the lattice scale follow the crystallographic orientation of their parental grains. We interpret our observation that the observed front irregularities (Fig. 2) and the characteristic width of the dehydration front (Fig. 4) are of similar size as the mean grain size (Table 1) as indirect evidence for the crystallographic control of dehydration at the grain scale.

We expect the orientation of gypsum grains to control the advance and organization of the dehydration front in a polymineralic gypsum rock (Fig. 14). In volumes that exhibit a high degree of fabric anisotropy, which Volterra alabaster does on the millimetre scale according to our analysis (Supplement, Fig. 1, Table 1), the dehydration should advance faster in the direction of the (010) lattice planes (Finot et al., 1997). We interpret our data to reflect such a pre-existing anisotropic fabric in part of the sample: (1) the orientation of pre-existing pores in the sample is highly anisotropic (Fig. 11a), and new pores follow this orientation (Fig. 11b, c); and (2) the progress of the dehydration front is highly asymmetric (Fig. 5a, c). A pre-existing fabric would also align grain boundaries and thermal-elastic damage. We interpret the observed plumes to map such zones of enhanced drainage.

Once the dehydration front has passed, the porosity consolidates rapidly and does not change significantly anymore. The cumulative pore size frequency distribution over time (Fig. 8) shows that, upon the initiation of dehydration, pores rapidly merge into a single cluster of interconnected pores (Fig. 9, Supplement, Fig. 4). This cluster connects the advancing reaction front with the outer surface of the unconfined sample.

Hildyard et al. (2011) describe networks of reacted and partly reacted material. They interpret the networks to delineate “large-scale fluid pathways” during the advance of a

SED
3, 857–900, 2011

dehydration front. The porous plumes we observed in our data are potentially related to these structures. A notable difference is that the plumes in our experiment encompass much smaller volumes compared to the networks in Hildyard et al.'s experiment (several hundreds of microns, cf. their Fig. 3b). However, we found no evidence that drainage in our sample is controlled by some sort of hierarchical porous network but rather by the interconnected pore cluster shown in Fig. 9 and Supplement, Fig. 4.

4.3 Data processing

The automated segmentation of grey scale images to isolate pores from their matrix is a critical processing step in the quantitative analyses of microtomographic data. Histogram-based thresholding is a rather simple method (Kaestner et al., 2008) and algorithms that utilize higher order information are generally favoured (e.g. Porter and Wildenschild, 2010, Wang et al., 2011). However, the intrinsic complexity of tomographic data generated from metamorphic rocks (which is constituted by the very large number of objects, their complicated shapes and wide range of size distributions, as well as the complex relationship to other phases) often renders advanced, feature-based techniques too difficult to use and computationally very expensive. Binary thresholding is a computationally efficient alternative.

All our SRμCT data suffer from an intrinsic discretization error, which arises from the use of cubic voxels to represent real objects (e.g. Arns et al., 2002). This error affects all volumetric analyses we conducted. We designed our shrinking/expansion experiment to assess the largest possible error resulting from discretization and emphasize that the error estimates provided are certainly exaggerated. We stress that the excellent coincidence of the determined porosities (24–25 %, Table 2) with the theoretically expected porosity (29 %, assuming no compaction) indicate that our approach and the thresholds we chose deliver very good first-order results.

SED
3, 857–900, 2011

5 Conclusions

Our in-situ Synchrotron X-ray microtomography experiment documents the dehydration of a 2.3 mm diameter cylinder of polycrystalline gypsum. Using a novel routine, we segment porosity from the tomographic time-series data on the basis of time-dependent changes to the grey value distribution that records the absorption of x-rays in the sample. Our workflow allows determining position, shape, volume and orientation of each individual pore and quantifying percolation over multiple scales. We show that the dehydration initiates at the margin of the unconfined cylinder. A sharp dehydration front slowly propagates radially inward over more than four hours and delimits an unreacted inner domain where no resolvable porosity forms. No run-away behavior is observed. In the inner domain, gypsum seems to be stabilized by increased pressures, which likely result from the thermal expansion of gypsum and locally increased pore fluid pressures. Across the dehydration front, gypsum breakdown is very efficient and most likely controlled by the orientation of the gypsum lattice with respect to the advancing front. We interpret the breakdown to occur where the pressure is relieved. Anisotropic pores form, whose non-random orientation can be explained by a preexisting fabric in the sample. Pores rapidly link to a large interconnected cluster of pores, that connects to the outside of the sample at all times, providing an efficient drainage pathway. We combine our observations in a model, in which the dehydration of polycrystalline gypsum is controlled by a feedback of pressure release and pore formation on the grain scale. In a companion paper (Karrech et al., 2011), we develop a theory that describes the advance of the dehydration front based on the dissipative mechanisms involved. The slow, strongly non-linear advance of the dehydration front can be fitted with a linear diffusion equation yielding a diffusivity of $8.29 \times 10^{-11}\ m^2\ s^{-1}$.

Supplementary material related to this article is available online at: http://www.solid-earth-discuss.net/3/857/2011/sed-3-857-2011-supplement.zip.

SED
3, 857–900, 2011

Acknowledgements. This work was supported by the Western Australian State Government through the Premier's Fellowship Program and the Western Australian Geothermal Centre of Excellence Program, and the Australian Synchrotron Research Program, funded by the Commonwealth of Australia under the Major National Research Facilities Program. Use of the Advanced Photon Source at Argonne National Laboratory was supported by the U. S. Department of Energy, Office of Science, Office of Basic Energy Sciences, under Contract No. DE-AC02-06CH11357. SLF acknowledges funding by NERC, grant NE/C002938/1, and by Spanish Ministerio de Ciencia e Innovación, grant RYC-2008-02067. CS acknowledges funding by the German Research Foundation under Grant No. SCHR 1262/1-1. We thank iVEC@UWA in Perth for use of their computing facilities. We thank S. Revets for making unpublished results available and K. Gessner, and R. Hough for help with data acquisition.

References

Arns, C. H., Knackstedt, M. A., Val Pinczewski, W., and Garnoczi, E. J.: Computation of linear elastic properties from microtomographic images: Methodology and agreement between theory and experiment, Geophysics, 67/5, 1396–1405, 2002.

Ballirano, P. and Melis, E.: Thermal behaviour and kinetics of dehydration of gypsum in air from in situ real-time laboratory parallel-beam X-ray powder diffraction, Phys. Chem. Min. 36, 391–402, 2009.

Banhart, J.: Advanced Tomographic Methods in Materials Research and Engineering, Oxford University Press, USA, 2008.

Bezou, C., Nonat, A., Mutin, J.-C., Christensen, A. N., and Lehmann, M. S.: Investigation of the crystal structure of γ-$CaSO_4$, $CaSO_4{\cdot}0.5\ H_2O$, and $CaSO_4{\cdot}0.6\ H_2O$ by powder diffraction methods, J. Solid State Chem, 117, 165–176, 1995.

Charola, A. E., Pühringer, J., and Steiger, M.: Gypsum: a review of its role in the deterioration of building materials, Environ Geol, 52, 339–352, 2007.

Christensen, A. N., Olesen, M., Cerenius, Y., and Jensen, T. R.: Formation and Transformation of Five Different Phases in the $CaSO_4$-H_2O System: Crystal Structure of the Subhydrate β-$CaSO_4{\cdot}\ 0.5\ H_2O$ and Soluble Anhydrite $CaSO_4$, Chem. Mater. 20, 2124–2132, 2008.

Clauser, C. and Huenges, E.: Thermal conductivity of rocks and minerals, in: Rock Physics

SED

3, 857–900, 2011

and Phase Relations, A Handbook of Physical Constants, AGU Reference Shelf 3, AGU, Washington, USA, 105–126, 1995.
Finot, E., Lesniewska, E., Mutin, J.-C., and Goudonnet, J.-P.: Reactivity of gypsum faces according to the relative humidity by scanning force microscopy, Surface Science, 384, 201–217, 1997.
Freyer, D. and Voigt, W.: Crystallization and Phase Stability of $CaSO_4$ and $CaSO_4$-Based Salts, Monatsh. Chem. 134, 693–719, 2003.
Freyer, D. and Voigt, W.: Can mixtures of α- and β-hemihydrates be quantified by means of thermoanalysis? ZKG Int. 62, 3, 47–53, 2009.
Hacker, B. R.: Diagenesis and fault valve seismicity of crustal faults, JGR 102, B11, 24459–24467, 1997.
Heard, H. C. and Rubey, W. W.: Tectonic implications of gypsum dehydration, Geol. Soc. Am.Bull., 77, 741–760, 1966.
Hildyard, R. C., Llana-Fúnez, S., Wheeler, J., Faulkner, D. R., and Prior, D. J.: Electron Backscatter Diffraction (EBSD) Analysis of Bassanite Transformation Textures and Crystal Structure Produced from Experimentally Deformed and Dehydrated Gypsum, J. Petrol., 52, 5, 839–856, 2011.
Jacques, S. D. M., González-Saborido, A., Leynaud, O., Bensted, J., Tyrer, M., Greaves, R. I. P., and Barnes, P.: Structural evolution during the dehydration of gypsum materials, Min. Magaz. 73, 3, 421–432, 2009.
Kaestner, A., Lehmann, E., and Stampanoni, M.: Imaging and image processing in porous media research, Adv. Water Resour., 31, 1174–1187, 2008.
Karrech, A., Regenauer-Lieb, K., Schrank, C., and Fusseis, F.: Dehydration of polycrystalline gypsum, a theoretical and numerical investigation based on first order thermodynamic principles, in prep., 2011.
Ko, S., Olgaard, D. L., and Wong, T.-F.: Generation and maintenance of pore pressure excess in a dehydrating system 1. Experimental and microstructural observations, JGR, 102, B1, 825–839, 1997.
Launeau, P., Archanjo, C. J., Picard, D., Arbaret, L., and Robin, P.-Y.: Two- and thre-dimensional shape fabric analysis by the intercept method in grey levels, Tectonophysics, 492, 230–239, 2010.
Liu, J., Regenauer-Lieb, K., Hines, C., Liu, K., Gaede, O., and Squelch, A.: Improved estimates of percolation and anisotropic permeability from 3-D X-ray microtomography using stochas-

SED
3, 857–900, 2011

tic analyses and visualization, Geochem. Geophy. Geosy., 10, doi:10.1029/2008GC002358, 2009.
Liu, J. and Regenauer-Lieb, K.: Application of percolation theory to microtomography of structured media: Percolation threshold, critical exponents, and upscaling, Phys. Rev. E, 83, 016106, doi:10.1103/PhysRevE.83.016106, 2011.
Llana-Fúnez, S., Brodie, K. H., Rutter, E. H. and Arkwright, J. C.: Experimental dehydration kinetics of serpentinite using pore volumetry, J. metamorphic Geol., 25, 423–438, 2007.
Llana-Fúnez, S., Wheeler, J., and Faulkner, D. R.: The influence of confining pressure during metamorphism: dehydration experiments with gypsum, Contrib. Mineral. Petr., in review, 2011.
McConnel, J. D. C., Astill, D. M., and Hall, P. L.: The pressure dependence of the dehydration reaction of gypsum, Mineral. Mag. 51, 453–457, 197.
Miller, S. A., van der Zee, W., Olgaard, D. L., Connoly, J. A. D.: A fluid-pressure feedback model of dehydration reactions: experiments, modeling, and application to subduction zones, Tectonophysics, 370, 241–251, 2003.
Murrel, S. A. F. and Ismail, I. A. H.: The effect of decomposition of hydrous minerals on the mechanical properties of rocks at high pressures and temperatures, Tectonophysics 31, 207–258, 1976.
Olgaard, D. L., Ko, S., and Wong, T.-F.: Deformation and pore pressure in dehydrating gypsum under transiently drained conditions, Tectonophysics, 245, 237–248, 1995.
Regenauer-Lieb, K. and Yuen, D.: Positive feedback of interacting ductile faults from coupling of equation of state, rheology and thermal-mechanics, PEPI, 142, 113–135, 2004.
Singh, N. B. and Middendorf, B.: Calcium sulphate hemihydrate hydration leading to gypsum crystallization, Prog. Cryst. Growth Ch., 53, 57–77, 2007.
Stauffer, D. and Aharony, A.: Introduction to Percolation Theory (2nd edition), Taylor & Francis Ltd., London, 1994.
Sprunt, E. S. and Brace, W. F.: Direct Observation of Microcavities in Crystalline Rocks, Int. J. Rock Mech. Min. Sci. & Geomech. Abstr. 11, 139–150, 1974.
Stock, S. R.: Microcomputed Tomography, Methodology and Applications, Taylor & Francis Ltd, London, 2009.
Stretton, I. C.: An experimental investigation of the deformation properties of gypsum, PhD thesis, Univ. Manchester, 1996.
Wang, W.-H. and Wong, T.-F.: Effects of reaction kinetics and fluid drainage on the development

SED
3, 857–900, 2011

of pore pressure excess in a dehydrating system, Tectonophysics 370, 227–239, 2003.
Wang, W., Kravchenko, A. N., Smucker, A. J. M., and Rivers, M. L.: Comparison of image segmentation methods in simulated 2-D and 3-D microtomographic images of soil aggregates, Geoderma, 162, 231–241, 2011.

SED
3, 857–900, 2011

Table 1. Grain size and anisotropy characterization of the sample material.

Grain size (micron)	Mean grain aspect ratio
82.9	1.524
69.9	1.262
122.7	1.277
104.8	1.089
45.2	2.173

SED
3, 857–900, 2011

Table 2. Porosities, total number of pores, the volume of the largest and second largest pore in the parallelepiped at different times during the experiment. See text for discussion.

Time (mins)	0	10	70	130	190	250	310
Porosity (%)	2.32	5.37	23.24	25.67	24.57	24.11	24.01
Total number pores	2 125 622	2 474 425	900 278	533 699	598 097	624 783	633 985
Size largest pore (vxl)	6612	1 752 795	37 255 760	43 514 600	41 093 659	40 067 000	39 831 390
Size 2nd largest pore (vxl)	3425	1 428 916	7881	2220	2579	3364	2226

SED
3, 857–900, 2011

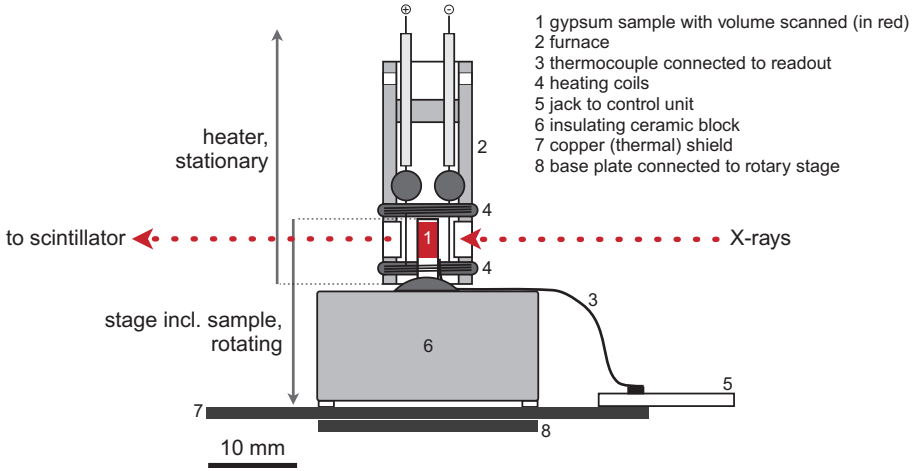

Fig. 1. To-scale sketch of the experimental set-up used within the X-ray beam configuration.

SED
3, 857–900, 2011

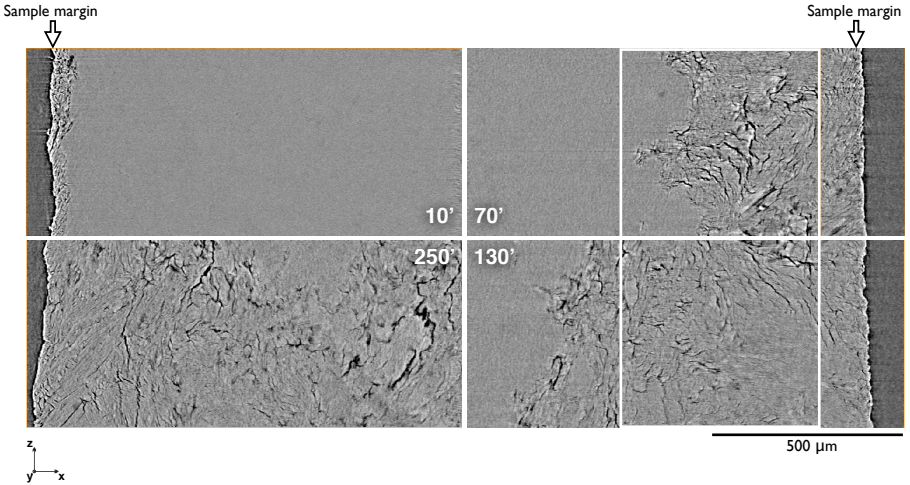

Fig. 2. Vertical cross section through the sample at different times during the experiment (depicted in the four quadrants). The grey values correspond to the absorption of X-rays, pores appear dark grey to black. The white stippled frame outlines the location of the parallelepiped in which porosity was quantified (see text and also Supplement, Fig. 5).

SED
3, 857–900, 2011

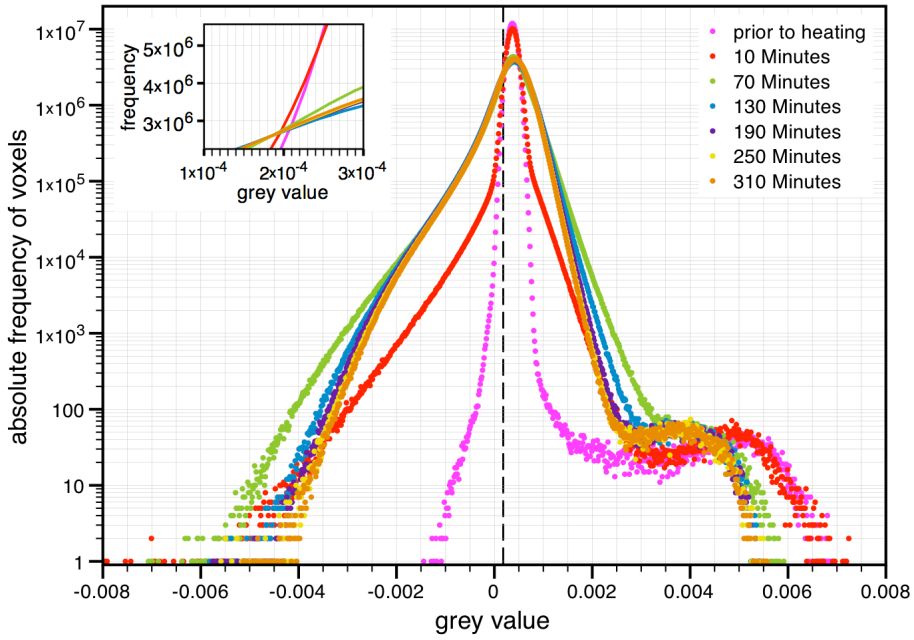

Fig. 3. Histograms of the grey value distributions amongst the $180x10^6$ voxel constituting the parallelepiped in which porosity was quantified, at different times during the experiment. The vertical stippled line indicates the critical threshold we used for segmenting porosity.

SED
3, 857–900, 2011

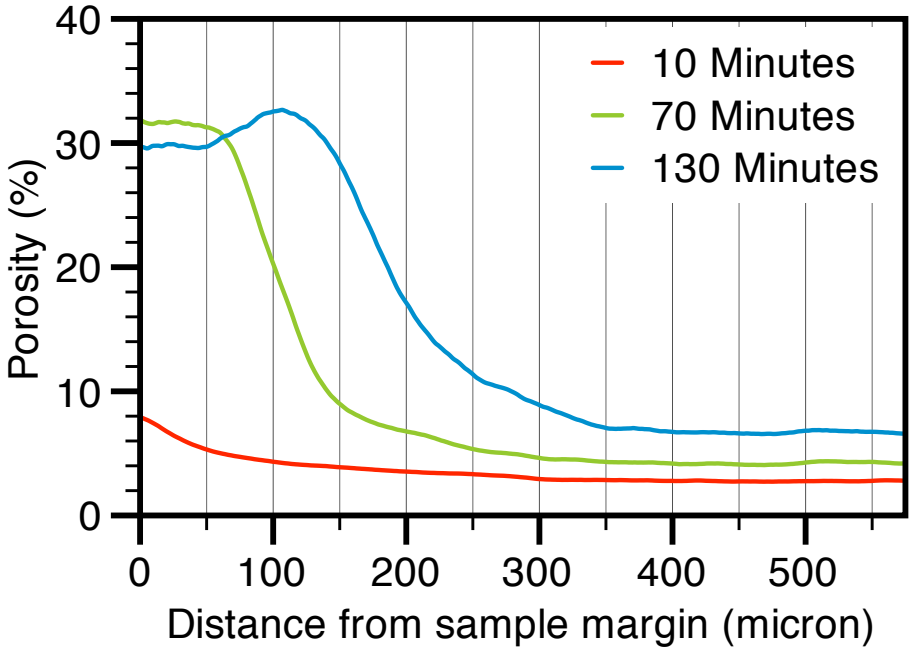

Fig. 4. Porosity evolution along a radius that crosscuts the dehydration front perpendicularly, at three different times during the experiment. Note the slightly increasing background porosity in the inner domain. Values exceeding 30 % porosity result from the comparatively small and non-representative sampling volume used to quantify porosity.

SED
3, 857–900, 2011

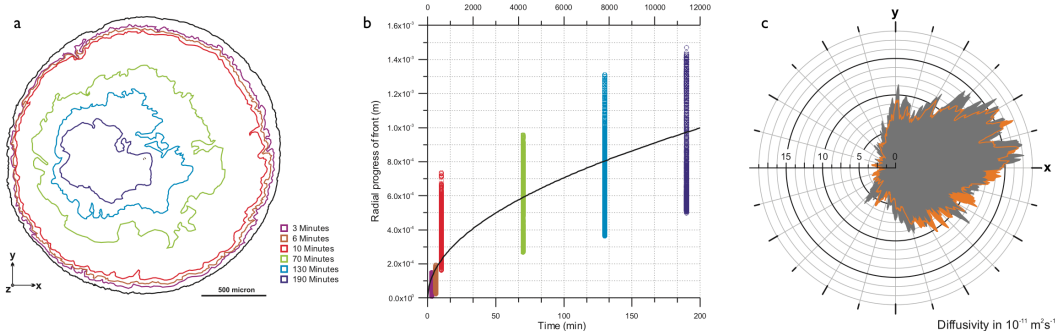

Fig. 5. The advance of the dehydration front, **(a)** the dehydration front in a horizontal section through the sample at different times during the experiment; **(b)** the position of the front in different directions over time quantified from horizontal and vertical sections through the sample. See text for explanation of the technique. c) rose plot of linear diffusion constants derived from fitting Eq. (1) to propagation of dehydration front along set of radii in two horizontal cross sections through the sample. Measurement strategy is explained in text (compare Supplement, Fig. 3).

SED
3, 857–900, 2011

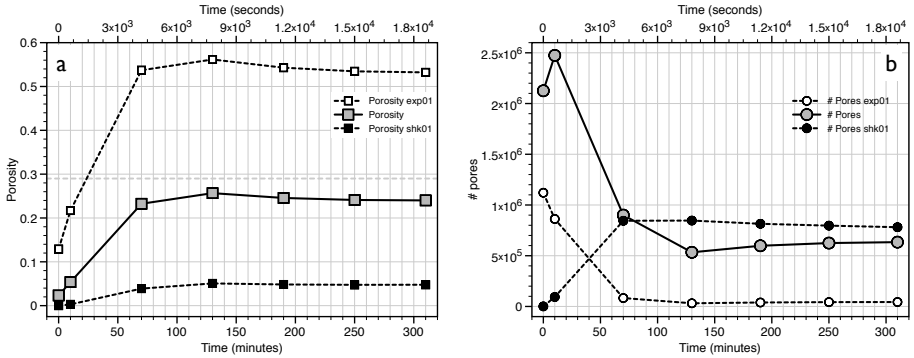

Fig. 6. Porosity quantification in the parallelepiped outlined in Fig. 2 and Supplement, Fig. 5; **(a)** Total porosity over time. Grey squares are the porosity values we determined using the threshold value derived from changes in the grey value histograms (Fig. 3). White and black squares, respectively, are the porosity values that resulted from the numerical expansion/shrinking experiment. **(b)** Total number of pores over time. White and black squares, respectively, are the total numbers of pores we derived from the numerical expansion/shrinking experiment. See text for explanation.

SED
3, 857–900, 2011

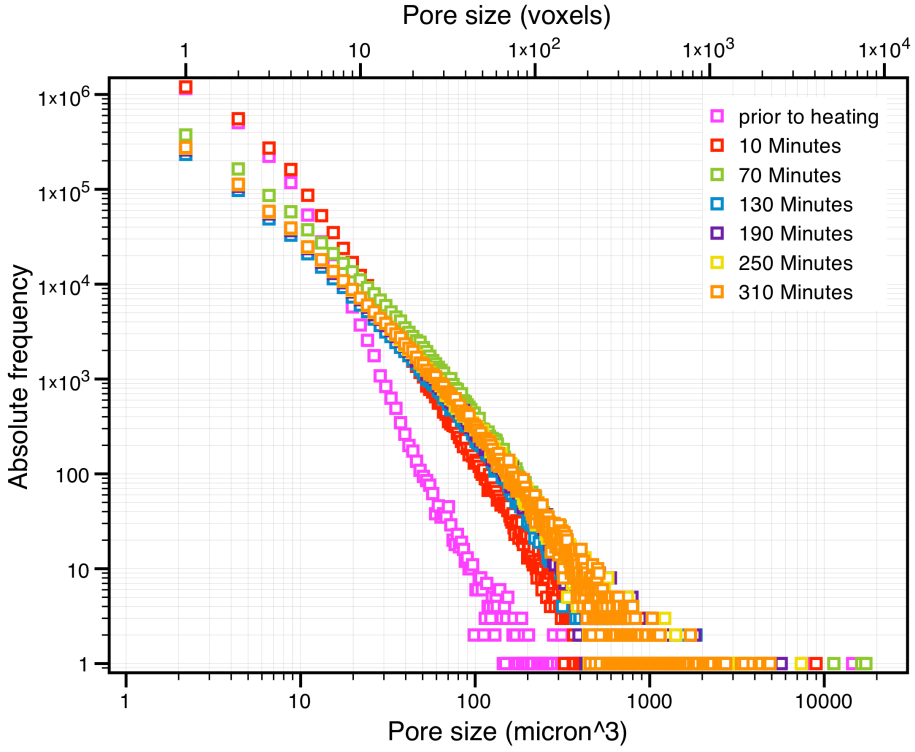

Fig. 7. Porosity size frequency distribution over time. See text for explanation.

SED
3, 857–900, 2011

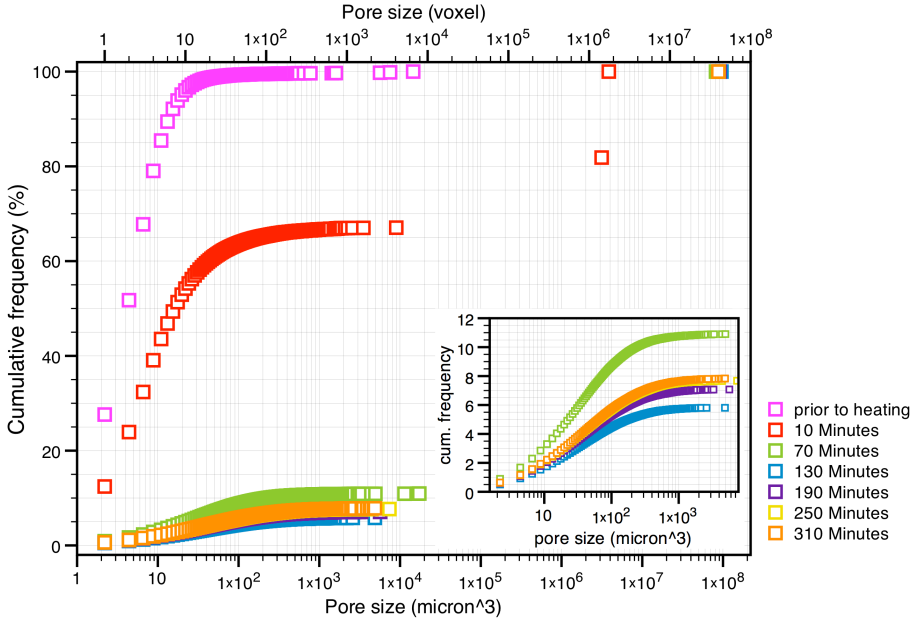

Fig. 8. Cumulative porosity size frequency distribution over time. See text for explanation.

SED
3, 857–900, 2011

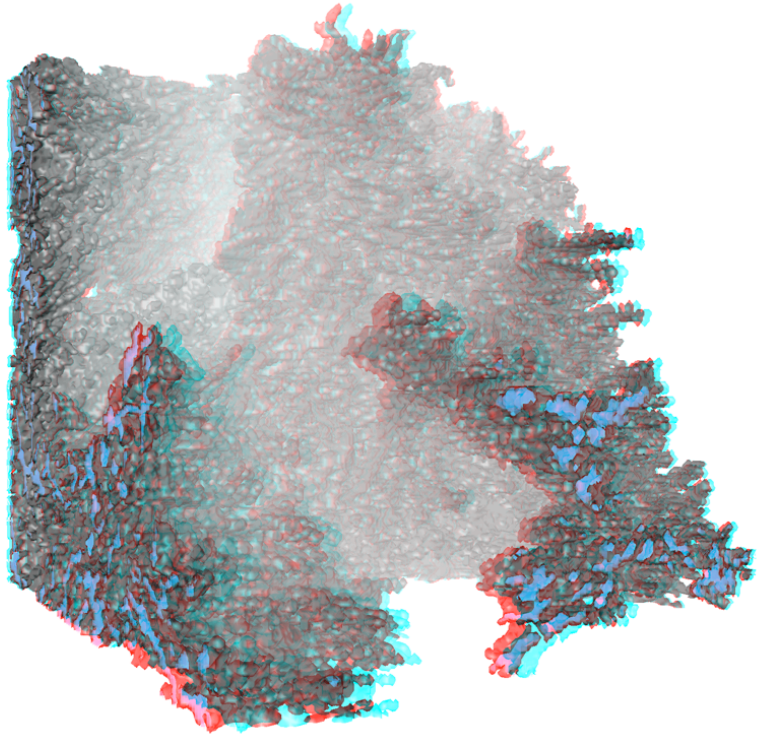

Fig. 9. Three-dimensional visualization of the morphology of the largest interconnected pore cluster at the reaction front – requires red-cyan glasses. Note the complexity of the pore shape. Side length of the cube shown is 200 voxel (260 µm).

SED
3, 857–900, 2011

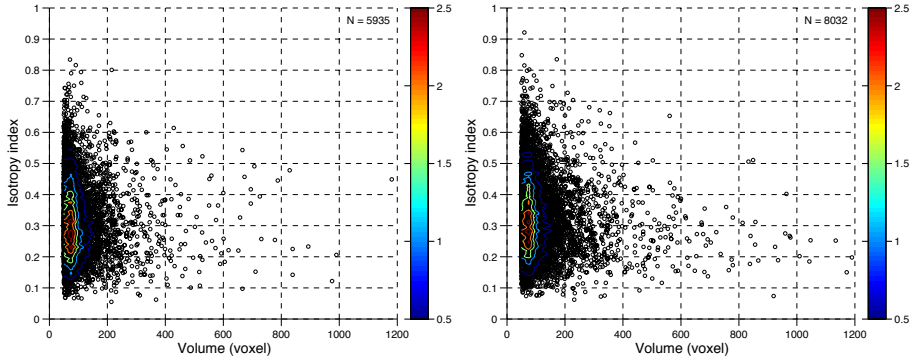

Fig. 10. Isotropy index over size of all pores [50; 1200 voxel], [110; 2640 µm^3] after 130 (left) and 310 min (right). Color-coded contours indicate data point density in percent (calculated for moving search windows of size 50 voxel × 0.01 isotropy index units for a step size of 25 voxel in horizontal direction and 0.005 isotropy index units in vertical direction).

SED
3, 857–900, 2011

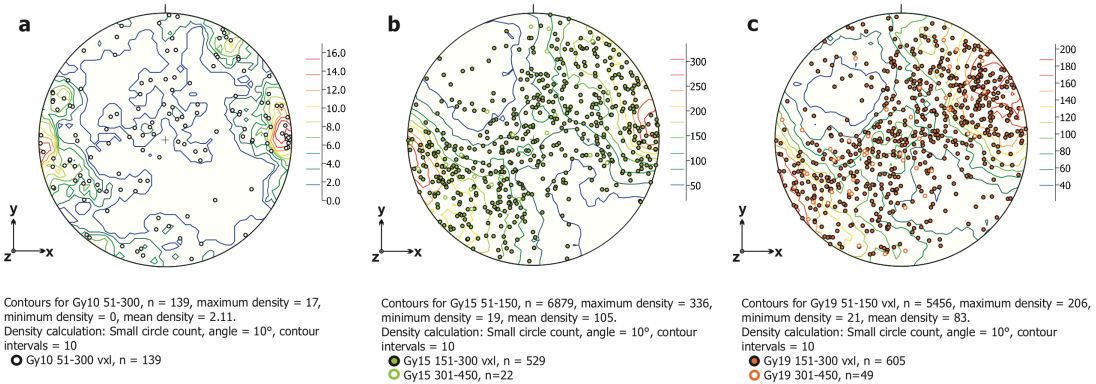

Fig. 11. Stereo plots showing the orientations of the longest principal axis of pores of different sizes. **(a)** Orientations prior to heating, contours calculated from pores between 51 and 300 voxel; **(b)** Orientations after 70 min, contours are calculated from pores between 51 and 150 voxel, black circles are orientations of pores between 151 and 300 voxel and green circles of pores between 310–140 voxel; and **(c)** Orientations after 310 min, contours are calculated from pores between 51 and 150 voxel, black circles are orientations of pores between 151 and 300 voxel and orange circles of pores between 310–140 voxel. See text for interpretation.

SED
3, 857–900, 2011

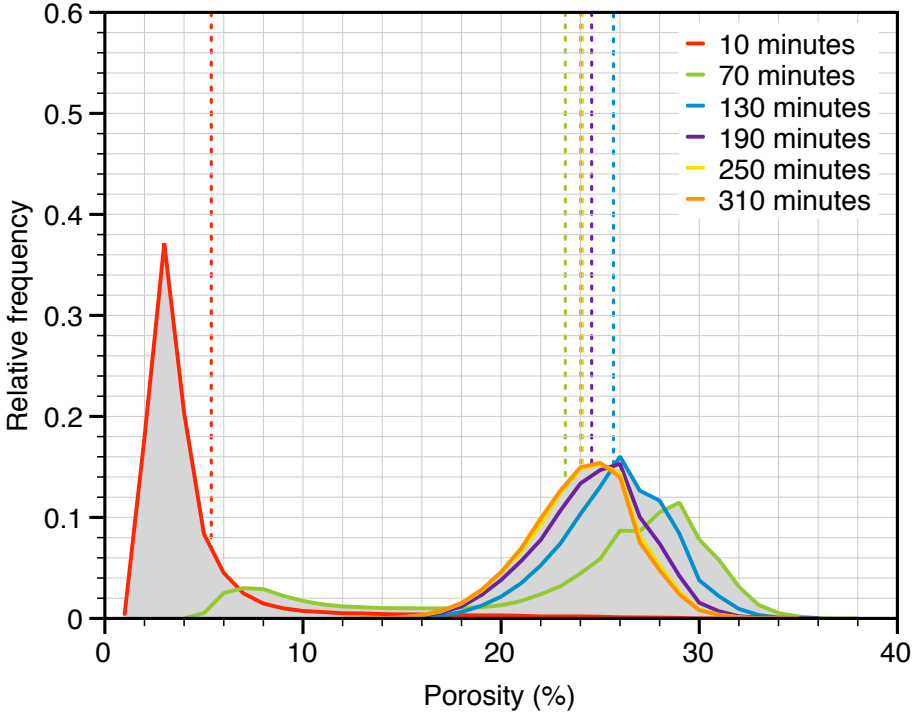

Fig. 12. Porosity frequency distribution amongst cubes with a 50-voxel side length placed in the parallelepiped at different times during the experiment (see text for explanation). Vertical lines mark the total porosity measured at different times.

SED
3, 857–900, 2011

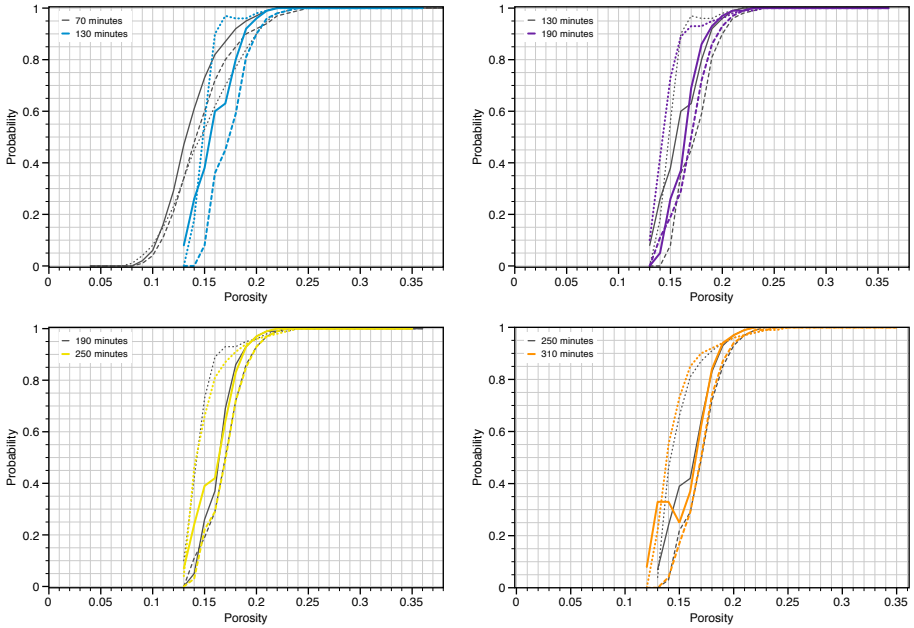

Fig. 13. Probability functions for percolation in the three principal directions amongst cubes with a 50-voxel side length placed in the parallelepiped. Each of the four diagrams compares two consecutive time steps. Dotted lines – x-axis, stippled line, y-axis, solid line – z-axis. Note that from 130 min onward, all cubes with more than about 22 % porosity are percolating in all three directions. In all cubes with a smaller porosity, the x-direction is most likely to percolate.

SED
3, 857–900, 2011

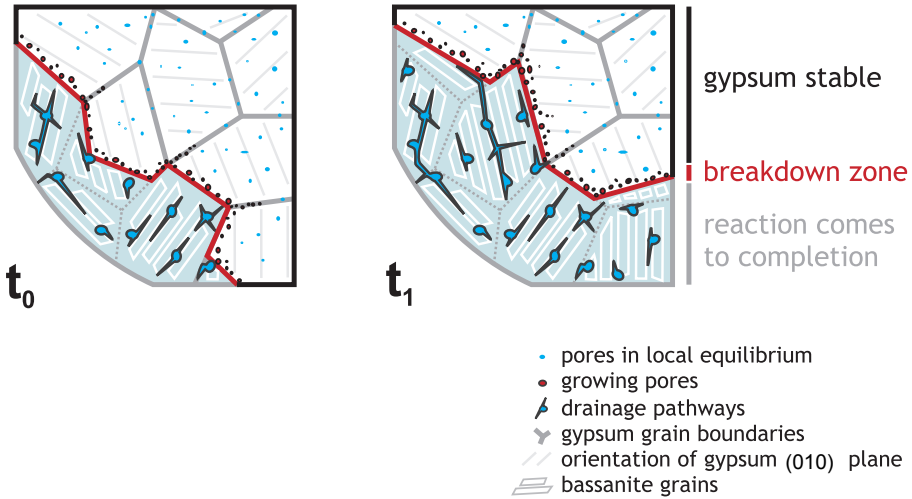

Fig. 14. Sketch map illustrating the grain-by-grain advance of the dehydration front and the effect of the strong crystallographic anisotropy of gypsum. See text for explanation.

SED
3, 857–900, 2011